



# Crystallization toughening of a model glass-ceramic

F.C. Serbena,<sup>a,\*</sup> I. Mathias,<sup>a</sup> C.E. Foerster<sup>a</sup> and E.D. Zanotto<sup>b</sup>

<sup>a</sup>Department of Physics, State University of Ponta Grossa (UEPG), 84.030-900 Ponta Grossa, PR, Brazil

<sup>b</sup>Vitreous Materials Laboratory (LaMaV), Department of Materials Engineering (DEMa), Federal University of São Carlos (UFSCar), 13.565-905 São Carlos, SP, Brazil

Received 26 September 2014; revised 25 November 2014; accepted 4 December 2014

**Abstract**—Lithium disilicates are commercially important and among the most widely studied and well-characterized glass-ceramics, but their toughening mechanism – and those of most glass-ceramics – is still unknown. In this work, stoichiometric lithium disilicate glasses were used as a model system and crystallized using carefully designed and controlled two-stage heat treatments to give different crystallized volume fractions while maintaining a constant grain size of approximately 12  $\mu\text{m}$ . This original procedure allowed us to separately control the effects of these two microstructural parameters on the mechanical properties of the glass-ceramic. The hardness, elastic modulus, four-point bending strength, indentation fracture toughness and double-torsion fracture toughness were measured for samples with different crystallized volume fractions, ranging from the parent glass to fully crystallized samples. We found that the bending strength increases rapidly with crystallization at crystal volume fractions below 10% and reaches a value 2.5 times greater than that of the original glass. For a fully crystallized sample, the fracture toughness increases almost fivefold, from 0.75 to 3.5  $\text{MPa}\cdot\text{m}^{1/2}$ . Laser confocal microscopy was used to reveal the topography of the fracture surfaces. Three mechanisms that contribute to toughening – crack deflection, crack bowing and trapping, and crack bridging – were evaluated. A model incorporating the elastic modulus, crystal fracture toughness and crystallized volume fraction was proposed and successfully tested to explain the increased fracture toughness with crystallized volume fraction for the full range of crystallization in  $\text{LS}_2$  glass-ceramics.

© 2014 Acta Materialia Inc. Published by Elsevier Ltd. All rights reserved.

**Keywords:** Glass-ceramics; Mechanical properties; Crystallization; Lithium disilicate; Fracture toughness

## 1. Introduction

Glass-ceramics result from the controlled crystallization of one or more crystalline phases embedded in a glassy matrix and normally have superior mechanical properties to non-ceramic glasses. By carefully controlling their composition and microstructure, several glass-ceramics have been designed for domestic and technological applications, such as bioactive implants [1], optical devices [2] and ultra-low thermal expansion materials [3–5].

One of the most successful commercially available glass-ceramics for dental applications is based on lithium disilicate ( $\text{LS}_2$ ) crystals. These commercial glass-ceramics typically contain a 50–80% volume fraction of 1–10  $\mu\text{m}$  lithium disilicate crystals embedded in a residual glass matrix. The crystals are lath shaped, forming a highly interlocked microstructure, which is responsible for their high mechanical strength. In the intermediate stages of crystallization, when lithium metasilicate crystals form, this glass-ceramic can be machined to desired shapes. An additional crystallization heat treatment forms  $\text{LS}_2$  and further increases the fracture strength. At the end of the crystalliza-

tion, the main crystalline phases are normally lithium disilicate and lithium metasilicate. The primary reasons for their high strength are thought to be their interlocked lath-shaped microstructure and the thermal expansion mismatch between the crystal and the glass matrix, which causes residual stresses that can contribute to crack deflection [6].

Some mechanical properties and residual stresses in stoichiometric  $\text{LS}_2$  glass-ceramics have already been measured and discussed [7–9]. However, these measurements were limited to relatively low crystallized volume fractions, or only the elastic modulus and bending strength were reported.

In this work, we performed an extensive investigation of a set of properties – hardness, elastic modulus, flexural strength, indentation fracture toughness and fracture toughness – of glassy to fully crystallized samples, while keeping the crystal size constant. We discuss the experimental results, considering the three main toughening mechanisms in glass-ceramics – crack deflection, crack bowing and trapping, and crack bridging. Finally, we propose and test a new model that successfully explains the observed data. To the best of our knowledge, this report is one of the most comprehensive and elucidative studies of mechanical properties as a function of microstructure while keeping the grain size constant reported for glass-ceramics.

\*Corresponding author. Tel.: +55 42 3220 3043; fax: +55 42 3220 3042; e-mail: [fserbena@uepg.br](mailto:fserbena@uepg.br)

## 2. Experimental procedure

A stoichiometric lithium disilicate ( $\text{Li}_2\text{O} \cdot 2\text{SiO}_2$ ) glass was prepared by mixing 260 g of the precursor powders ( $\text{Li}_2\text{CO}_3$ ; Vetec) and  $\text{SiO}_2$  (Vitrovita; Quartz 2) in a rotating polyethylene bottle for 2 h and then melting in a platinum crucible at 1400 °C for 2 h in an electric furnace in air. The melt was cast between massive steel plates, and the resulting glass pieces of  $60 \times 30 \times 25 \text{ mm}^3$  were annealed at 440 °C (15 °C below the glass transition temperature,  $T_g$ ) for 30 min to partially relieve the residual thermal stresses. The samples were cut using a diamond saw, polished using silicon carbide paper up to 1200 grit and finished with a cerium oxide suspension. After polishing, all samples were submitted to thermal treatment at 435 °C for 2 h to relieve the stresses induced by the cutting and polishing procedures.

Crystallization was performed using a two-stage heat treatment, the first for nucleation and the second for crystal growth. These heat treatments were performed in an electric furnace with the temperature controlled to within  $\pm 1$  °C. The nucleation and growth temperatures were 455 and 560 °C, respectively. The nucleation time was varied to obtain different crystallized volume fractions, whereas the growth period was held constant to obtain crystals with the same diameter. All samples had a very narrow size distribution (this narrow distribution is very important for the correlation of fracture strength and toughness with crystallized volume fraction, described later in this article). The crystallized volume fraction was evaluated by analyzing several optical micrographs using the software ImageJ [10]. At least 500 crystals were observed to ensure a good ensemble. The crystals revealed themselves in the microstructure after exposure to air for a few days due to the differential effects of humidity on the crystals and the residual glass matrix.

The  $T_g$  was measured using a differential scanning calorimeter (DSC; model DSC 404, Netzsch), with a heating rate of  $10 \text{ °C min}^{-1}$ . The thermal expansion coefficient of the glass ( $\alpha_g$ ) and glass-ceramic samples with different volume fractions ( $\alpha_{gc}$ ) were obtained using a Netzsch DIL 402PC dilatometer in the temperature range from 40 to 430 °C.

The crystalline phases were identified using X-ray diffraction and a Rigaku Ultima IV X-ray diffractometer. The X-ray spectra were obtained in samples with different crystallized volume fractions using Cu  $K_\alpha$  radiation in the  $\theta$ – $\theta$  configuration. The diffraction peaks were measured from  $2\theta = 10^\circ$  to  $80^\circ$  in  $0.02^\circ$  steps at room temperature.

The hardness ( $H$ ) and elastic modulus ( $E$ ) of the glass and glass-ceramic samples were measured using instrumented indentation with a Nanoindenter XP™ indenter (MTS Instruments) with a Berkovich diamond tip. The maximum applied load was 400 mN in 10 loading–unloading cycles. A matrix of 25 indentations was made in each sample, and the values of  $H$  and  $E$  were calculated following the procedure of Oliver and Pharr [11]. Therefore, the values of  $H$  and  $E$  are the averages for each group of indentations.

Conventional microindentation tests were also performed using a Microindenter Leica VMHT MOT with a dwell time of 15 s at room temperature. The applied loads were 5 and 10 N. These loads were able to produce well-defined radial cracks in the glass and crystallized samples. A total of five indentations were performed for each load. The radial crack lengths and indentation diagonals were

measured no more than 15 min after the indentations tests using an optical microscope. The indentation fracture toughness ( $K_{IC}$ ) values were calculated using the models of Niihara et al. [12] and Anstis et al. [13] according to the following equations:

$$\left[ \frac{K_{IC} \phi}{Ha^{1/2}} \right] \left( \frac{H}{E\phi} \right)^{2/5} = 0.129 \left( \frac{c}{a} \right)^{-3/2} \quad (1)$$

$$K_{IC} = 0.016 \sqrt{\frac{E}{H}} \left( \frac{P}{c^{3/2}} \right) \quad (2)$$

where  $a$  is the half-diagonal impression,  $2c$  the radial crack length and  $\phi$  a constant equal to 3. In all measurements,  $c/a \geq 2.5$ .

The bending strengths of the glasses and glass-ceramics were determined using a four-point bend jig. The jig and rollers were made of stainless steel. The separations between the inner and outer rollers were 10 and 20 mm, respectively. The sample dimensions were approximately  $30 \times 2 \times 2 \text{ mm}^3$ . Their preparation involved cutting, grinding and polishing in an aqueous  $\text{CeO}_2$  solution. The final surfaces were smooth and well polished. The load was applied in compression mode using a universal mechanical testing machine (Shimadzu AGS-X 5kN) with a constant displacement rate of  $2 \text{ mm.min}^{-1}$  and transferred to the sample jig using an alumina sphere. A total of three samples were tested for each crystallized volume fraction and the results are the average of these tests. The crystallized surface layer was removed by polishing prior to testing. The final polishing was made in an aqueous  $\text{CeO}_2$  solution. For one set of fully crystallized samples, the tests were performed without removing the crystallized surface layer to investigate the effect of the surface crystallization on the bending strength.

The flexural strength  $\sigma_s$  was calculated according to Ref. [14]:

$$\sigma_s = \frac{3P\delta}{Wt^2}, \quad (3)$$

where  $\delta = (l_1 - l_0)/2$ ,  $l_0$  and  $l_1$  being the inner and outer roller separations, respectively,  $P$  is the applied load at fracture,  $t$  is the specimen thickness and  $W$  is the specimen width.

The fracture toughness ( $K_{DTIC}$ ) of the glass and glass-ceramic samples was measured using the double torsion technique at room temperature in air [15]. Sample plates of  $30 \times 15 \times 1.5 \text{ mm}^3$  were cut and their surfaces polished. A 10 mm long, 450  $\mu\text{m}$  wide notch was introduced using a diamond disk. An inclined tip was produced inside the notch parallel to the major axis using the diamond disk and a sharp crack produced by a 10 N load Vickers indentation was introduced near the notch tip surface to guide the initial crack [16]. The testing apparatus consisted of a jig and a universal testing machine (Shimadzu AGS-X 5kN). A schematic view of the experimental apparatus is shown in Fig. 1. The jig consisted of four stainless steel spheres, all of 3 mm radius, fixed onto a plate and separated by 11 mm in width and 20 mm in length. An alumina sphere with a 5 mm radius was placed between the edges of the notch and used to apply the compression load, forming a bending arm with the lower spheres of 5.5 mm. Previous testing at a displacement rate of  $0.01 \text{ mm min}^{-1}$  was applied to promote crack growth. Finally, the load was

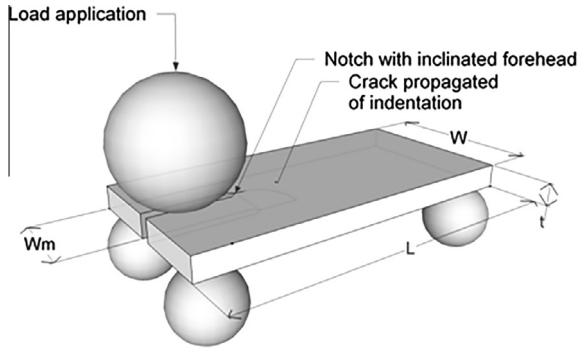


**Fig. 1.** Schematic view of the double torsion apparatus used in this work.

applied at a displacement rate of  $2 \text{ mm} \cdot \text{min}^{-1}$  for the determination of  $K_{\text{DTIC}}$ . The samples were stress relieved before and after the introduction of the notch by annealing at  $435 \text{ }^\circ\text{C}$  for 2 h and cooling at a rate slower than  $1 \text{ }^\circ\text{C} \cdot \text{min}^{-1}$ . The aim of the heat treatment before the notch introduction was to ensure that the sample would not fracture during notching. Additionally, the aim of the heat treatment after the notch was introduced was to ensure that a straight crack would be produced. The experiments showed that if the stresses were not relieved, the crack path would not be straight. The fracture toughness  $K_{\text{DTIC}}$  was calculated according to Refs. [17,18]:

$$K_{\text{DTIC}} = P_C W_m \sqrt{\frac{3}{W t^4 (1 - \nu) \psi}} \quad (4)$$

where  $W_m$  is the moment arm,  $\nu$  is the Poisson's ratio,  $P_C$  is the load at fracture and  $\psi$  is equal to  $1 - 0.6302\tau + 1.20\tau \exp(-\pi/\tau)$ , where  $\tau = 2t/W$ .

Before any mechanical test, such as hardness or indentation fracture toughness, all samples were treated at  $435 \text{ }^\circ\text{C}$  for 2 h and cooled at a rate slower than  $1 \text{ }^\circ\text{C} \cdot \text{min}^{-1}$  to room temperature to relieve any surface residual stress caused by the machining of the specimens. The internal residual stresses owing to the mismatch between the crystals and the residual glass phases cannot be relieved.

Surface scanning profiles of the fractured surfaces of the double torsion test samples were obtained using a laser confocal microscope (LEXT OLS4100) with a  $20\times$  objective lens. These profiles were measured on different regions of the fractured surface. They were  $250 \mu\text{m}$  in length and aligned in the direction of the specimen length. The crack angle at each point was determined based on the derivative of the profile. The crack deflection angle distributions were calculated as a function of the crystallized volume fraction.

### 3. Results

#### 3.1. Crystallization and thermal properties

Fig. 2(a) and (b) show crystals nucleated in the samples with 32 and 84% crystallized volume fractions, respectively, after the removal of the crystallized surface layer. The crystals are slightly elongated, with a 1.6:1 aspect ratio, and the long axis is  $12 \mu\text{m}$ .

Fig. 3 shows a DSC trace of the glass measured as a monolithic piece. The glass transition temperature is

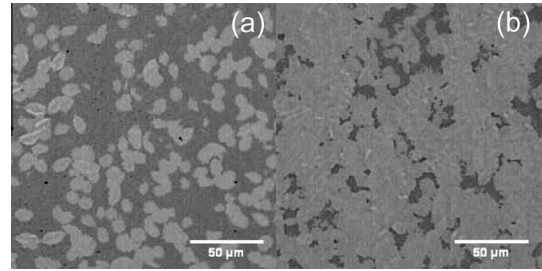


**Fig. 2.** Crystallized  $\text{LS}_2$  samples treated for (a) 42 h and (b) 72 h at  $455 \text{ }^\circ\text{C}$  for crystal nucleation and 55 min at  $535 \text{ }^\circ\text{C}$  for crystal growth, corresponding to crystallized volume fractions of 32 and 84%, respectively.

$455 \text{ }^\circ\text{C}$  (onset), which is very close to the  $T_g$  of other reported stoichiometric lithium disilicate glasses (e.g. [19,20]). One exothermic crystallization peak and one endothermic peak, corresponding to the fusion of the crystallized glass, are also observed.

Thermal expansion data obtained via dilatometry for a glassy and a fully crystallized sample are shown in Fig. 4. The linear thermal expansion was calculated using a linear regression fitting of the thermal expansion curves. Average linear thermal expansion coefficients of  $12.2 \times 10^{-6} \text{ }^\circ\text{C}^{-1}$  for the glass sample ( $\alpha_g$ ) and  $10.1 \times 10^{-6} \text{ }^\circ\text{C}^{-1}$  for the fully crystallized sample ( $\alpha_c$ ) were obtained. These values are in good agreement with the literature values. For instance, Freiman and Hench [7] reported a thermal expansion coefficient of  $12.5 \times 10^{-6} \text{ }^\circ\text{C}^{-1}$  for a glass and one of  $10.0 \times 10^{-6} \text{ }^\circ\text{C}^{-1}$  for a fully crystallized sample. Similarly, Mastelaro and Zanotto [8] obtained  $12.8 \times 10^{-6} \text{ }^\circ\text{C}^{-1}$  for a glass and  $10.8 \times 10^{-6} \text{ }^\circ\text{C}^{-1}$  for a fully crystallized  $\text{LS}_2$  sample.

X-ray diffraction of a fully crystallized sample allowed for the determination of the crystal phases, and the resulting spectrum is shown in Fig. 5. The only crystallized phase was  $\text{Li}_2\text{Si}_2\text{O}_5$ , which has an orthorhombic unit cell belonging to the  $Ccc2$  space group [21].

#### 3.2. Mechanical properties

##### 3.2.1. Hardness and elastic modulus

Fig. 6(a) shows the hardness obtained from instrumented indentation experiments as a function of the crystallized volume fraction ( $f$ ). The hardness increases

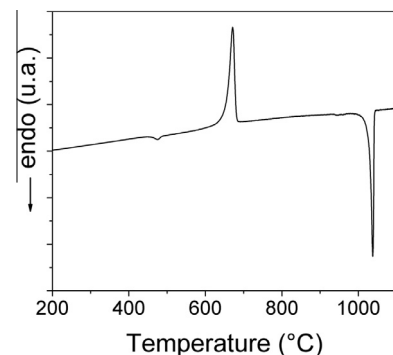


**Fig. 3.** DSC trace of the  $\text{LS}_2$  glass used in this study. The glass transition temperature was  $455 \text{ }^\circ\text{C}$ , the crystallization onset occurred at  $653 \text{ }^\circ\text{C}$  and the melting onset occurred at  $1026 \text{ }^\circ\text{C}$ .

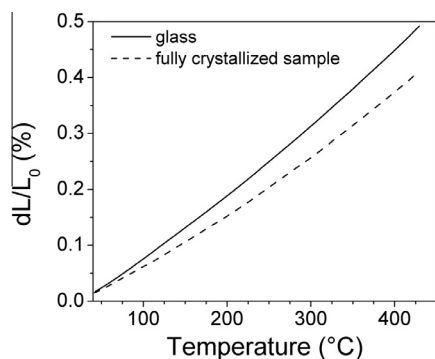


Fig. 4. Dilatometric curves for glass and fully crystallized samples.

linearly with the crystallized volume fraction. The hardness of the glass is  $6.5 \pm 0.2$  GPa and that of the fully crystallized sample is  $8.3 \pm 0.6$  GPa, showing an increase of approximately 28%.

Fig. 6(b) shows the elastic modulus as a function of the crystallized volume fraction. The elastic modulus is  $80 \pm 2$  GPa for the glass and  $133 \pm 5$  GPa for the fully crystallized glass-ceramic. As observed for the hardness, the dependence of the elastic modulus increases linearly with the crystallized volume fraction. Massardo [22] also measured the hardness and elastic modulus of stoichiometric  $LS_2$  glass-ceramics using instrumented indentation. However,  $H$  and  $E$  were only determined for low crystallized volume fractions, up to 10%, and for a fully crystallized sample, not for intermediate or higher crystallized volume fractions. Our values agree with those in Ref. [22]. Mastelaro and Zanotto [8] also determined the elastic modulus of a glass and a fully crystallized glass-ceramic using an ultrasonic technique. They obtained values of 71 and 122 GPa for the glass and glass-ceramic, respectively. These values are similar to ours.

### 3.2.2. Flexural strength

Samples with different crystallized volume fractions and with the crystallized surface layer removed were tested in a four-point bending experiment. Fig. 7 shows the results for glass-ceramics with different crystallized volume fractions,  $f$ . The glass flexural strength was  $103 \pm 3$  MPa, while the fully crystallized sample had a flexural strength of  $260 \pm 20$  MPa – a notable increase of 150%. The largest increase in the flexural strength was observed for low values of  $f$ . For highly crystallized samples, the increase was almost linear with  $f$ . Fully crystallized samples for which

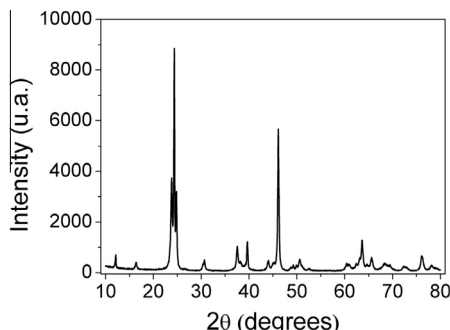


Fig. 5. X-ray diffraction pattern of a fully crystallized sample showing only  $LS_2$  crystals.

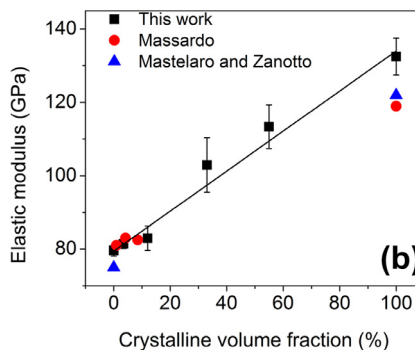
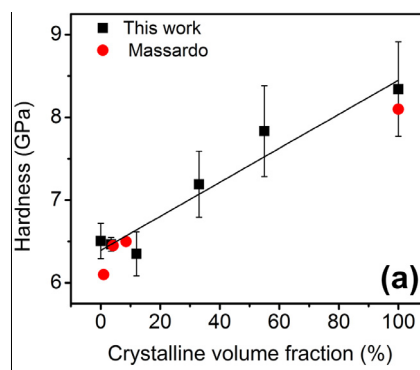


Fig. 6. (a) Hardness and (b) elastic modulus as a function of crystallized volume fraction, as measured using instrumented indentation. The lines are a linear fit of the data ( $r^2 = 0.88$  and  $0.98$ , respectively).

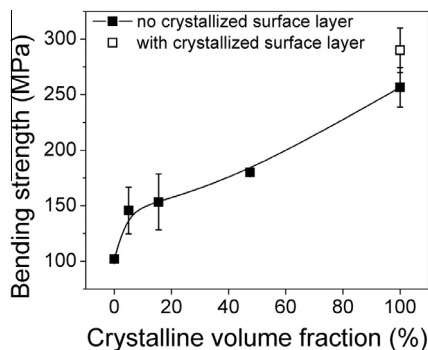


Fig. 7. Four-point bending strength of  $LS_2$  glass-ceramic samples as a function of crystallized volume fraction. The line is only a guide to the eye.

the crystallized surface layer was not removed were also tested. These samples had an even greater flexural strength,  $290 \pm 20$  MPa, which is in agreement with other reported values [23–25].

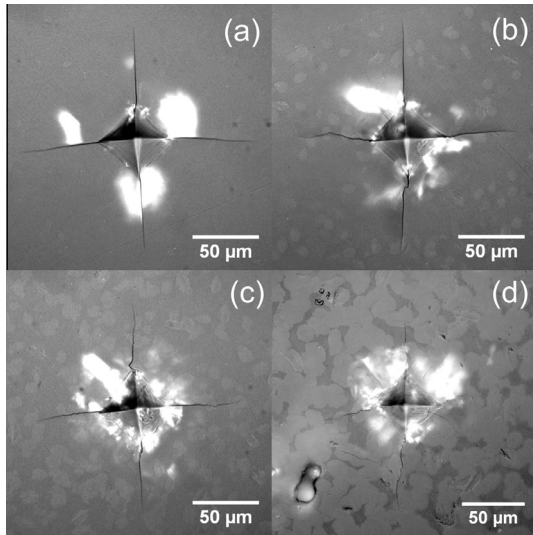
We checked for the presence of defects near the fracture surfaces of the samples used for the flexural strength tests and observed the presence of pores. The results are indicated in Table 1. Pores often nucleate and grow in glass-ceramics due to density mismatches between the residual glass and the crystal phase, and also due to the expulsion of dissolved gases at the crystal/glass interface.

### 3.2.3. Indentation fracture toughness

Fig. 8(a)–(d) show images of 10 N Vickers indentations in the 3, 12, 33 and 84% partially crystallized  $LS_2$  samples.

**Table 1.** Porosity and pore size as a function of crystallized volume fraction from the flexural strength tests.

Crystal fraction $f$ (%)	Porosity (%)	Pore radius ( $\mu\text{m}$ )
16	0.4	$9 \pm 5$
48	3	$15 \pm 5$
100	5	$13 \pm 5$

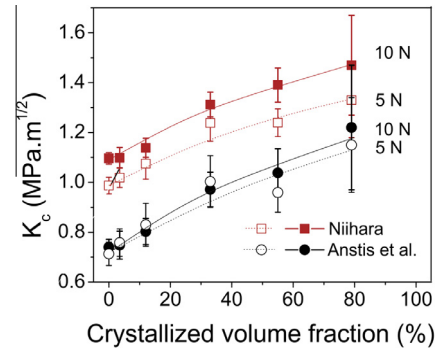
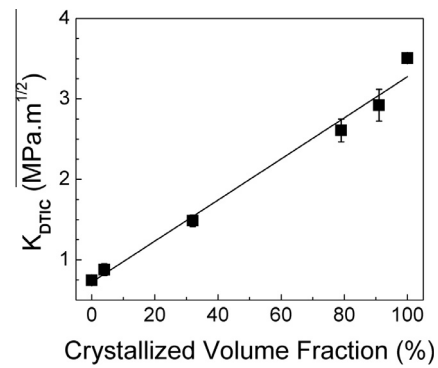
**Fig. 8.** Optical micrographs of Vickers indentations in the (a) 3%, (b) 12%, (c) 33% and (d) 79% crystallized samples with a 10 N applied load.

As the crystallized volume fraction increases, the cracks changed their propagation direction following the energetically most favorable path. The fracture plane passes through some precipitates via cleavage, most likely along the planes that have the lowest surface energy. The indentation diagonals ( $2a$ ) and lengths of the radial cracks ( $2c$ ) were used to calculate the toughness following the Niihara et al. [12] and Anstis et al. [13] models. The white spots observed in the photographs are reflections of the microscope light by lateral cracks below the surface.

Fig. 9 shows the indentation fracture toughness according to the models of Niihara et al. and Anstis et al. (Eqs. (1) and (2)). This type of fracture toughness increases continuously with the crystallized volume fraction. Reliable data for the fully crystallized sample to calculate the indentation fracture toughness could not be obtained because several cracks were formed around the indentation, preventing accurate measurement. The results obtained using the Niihara et al. model showed a dependence on the applied load, which was higher for the 10 N load than for the 5 N load. The Anstis et al. model showed a smaller load dependence. Additionally, the  $K_C$  calculated using the Anstis et al. model was approximately 20% lower than that determined using the Niihara et al. model.

### 3.2.4. Fracture toughness

The fracture toughness values,  $K_{DTIC}$ , of the glass-ceramics were obtained using the double torsion technique. Fig. 10 shows the values of  $K_{DTIC}$  as a function of the crystallized volume fraction. For the parent glass sample,  $K_{DTIC}$  was  $0.75 \pm 0.01 \text{ MPa}\cdot\text{m}^{1/2}$ , the most typical value for silicate glasses. Crystallization increased the  $K_{DTIC}$  up

**Fig. 9.** Indentation fracture toughness as a function of crystal volume fraction according to the Niihara et al. and Anstis et al. models for 5 and 10 N loads. The lines are only guides to the eye.**Fig. 10.** Fracture toughness of  $\text{LS}_2$  glass and glass-ceramics as a function of crystallized volume fraction. The line is a linear fit with  $r^2 = 0.98$ .

to  $3.50 \pm 0.05 \text{ MPa}\cdot\text{m}^{1/2}$  for the fully crystallized sample, which is approximately five times greater than the value for the glass. Fig. 10 shows that the  $K_{DTIC}$  dependence with  $f$  is almost linear.

**3.2.4.1. Study of the fracture surfaces.** The surface profiles of the fracture surfaces were measured using a laser confocal microscope. Representative images of the fracture surfaces are shown in Fig. 11(a)–(d). The surface roughness increased with  $f$  due to crack deflection. Additionally, the fracture plane cut most of the precipitates. Segments of the crack surfaces were mapped. In the sample with a 32% crystallized volume fraction, crack deflection is evident and is associated with the change in crack path when it encounters a crystal. In the fully crystallized sample, the amount of crack deflection is much greater.

To quantitatively treat crack deflection, crack profiles were measured, and the results for all tested samples are shown in Fig. 12. Crack deflection becomes more significant as the crystallized volume fraction increases.

The crack deflection angle distribution was calculated from the derivative of the crack profile at each point. The distributions as functions of the crystallized volume fraction are shown in Fig. 13(a), and their respective cumulative probabilities are shown in Fig. 13(b). The distributions are unimodal and the median increases with the crystallized volume fraction, from  $0.9^\circ$  for the glass to  $18.7^\circ$  for the fully crystallized sample. These distributions

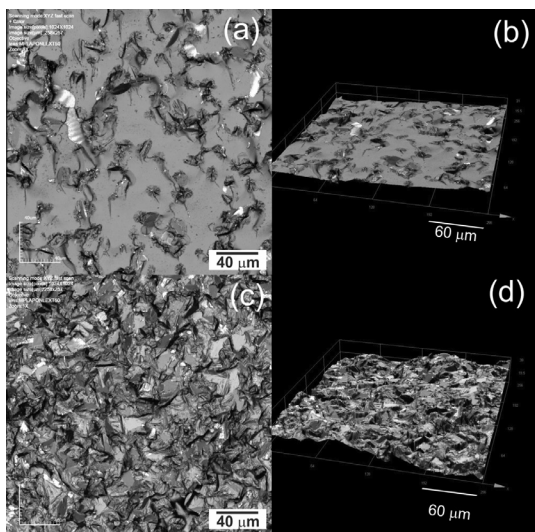


**Fig. 11.** Laser confocal micrographs of fracture surface segments of  $LS_2$  samples with  $f = 32\%$ : (a) top view and (b) perspective view; and samples with  $f = 100\%$ : (c) top view and (d) perspective view.

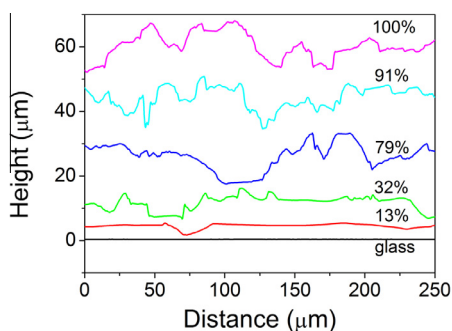


**Fig. 12.** Crack profiles of the fracture surfaces of the tested double torsion samples for the different crystallized volume fractions.

will be used in the discussion to estimate the increase in fracture toughness due to the crack deflection.

## 4. Discussion

### 4.1. Mechanical properties

#### 4.1.1. Hardness and elastic modulus

The indentation technique is widely used to determine the mechanical properties of glasses and glass-ceramics. To the best of our knowledge, there have been no reported studies about the mechanical properties of these glass-ceramics with systematic variations in the crystallized volume fraction with a constant crystal size. Most previous studies refer to fully crystallized glass-ceramics or low crystallized volume fractions. For instance, using instrumented indentation, Massardo [22] obtained hardnesses of  $5.8 \pm 0.5$  and  $8.0 \pm 0.6$  GPa for the glass and fully crystallized samples, respectively. The elastic modulus was also measured, and the values were  $78 \pm 2$  and  $83 \pm 6$  GPa for the glass and the fully crystallized glass-ceramic, respectively. Mastelaro and Zanotto [8], using an ultrasonic technique, obtained an elastic modulus of 75 GPa for the glass and 122 GPa for a fully crystallized glass-ceramic sample.

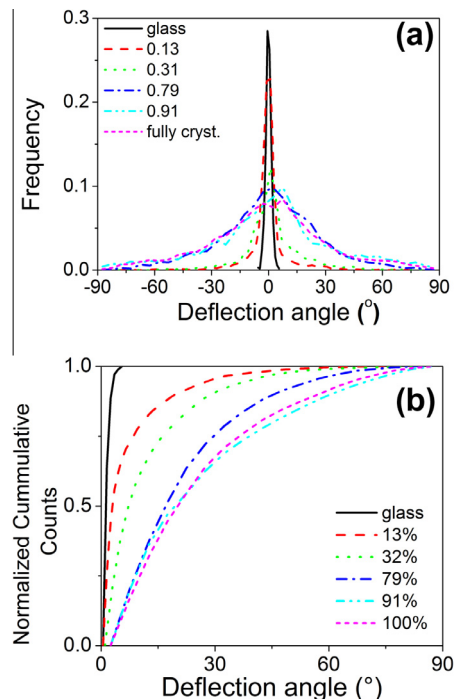


**Fig. 13.** (a) Distribution of the crack deflection angles for various crystallized volume fractions; (b) cumulative counts of deflection angles for glass-ceramics with distinct crystallized fractions (with a constant crystal size of 12  $\mu\text{m}$ ).

Using instrumented nanoindentation, Buchner et al. [26] reported 6.2 and 82 GPa for the hardness and elastic modulus, respectively, of  $LS_2$  glass.

Similarly, the hardness of lithium disilicate-based (non-stoichiometric) glass-ceramics has been measured. For the commercial EMPRESS 2™ used for dental applications, which has  $Li_2Si_2O_5$  as the main crystallized phase, Vickers hardnesses in the range 5.3–5.5 GPa for a crystallized volume fraction of 65% were reported [27]. Its microstructure consists mainly of elongated crystals of lithium disilicate that are 5  $\mu\text{m}$  in length and have a 7:1 aspect ratio.  $12Li_2O-79SiO_2-4K_2O-5Al_2O_3$  wt.% glass-ceramics showed a Vickers hardness of 5.3 GPa [28]. However, higher hardness values, ranging from 8.1 to 8.4 GPa, have also been observed for off-stoichiometric  $LS_2$  glass-ceramics with small amounts of Al, P and Zr [29]. Vickers hardness values of non-stoichiometric  $LS_2$  glass-ceramics containing small amounts of Ca, P and Zr and with a crystallized volume fraction of 60–65% were in the range 6.4–7.8 GPa [20]. All of these values are in the range of those measured in this work for stoichiometric  $LS_2$  glass-ceramics. While the Vickers hardness is defined as the applied load to contact area ratio, the Berkovich hardness is defined as the applied load to projected area ratio. Vickers hardness is typically  $\sim 7\%$  lower than the hardness measured using a Berkovich indenter.

The elastic modulus of  $LS_2$ -based glass-ceramics with additions of other elements has also been measured. Borom et al. [30] obtained 70 GPa for the elastic modulus of the glass and a maximum of 90 GPa for glass-ceramics with a 50% crystallized volume fraction. The elastic modulus measured for EMPRESS 2™ is in the range of 90–96 GPa [27,31,32]. Apel et al. [33] measured an elastic modulus of 108 GPa for a  $SiO_2-Li_2O-K_2O-Al_2O_3-P_2O_5$  glass-ceramic with a 60% crystallized volume fraction of  $Li_2Si_2O_5$ , the

main crystalline phase. Finally, Deubener et al. [34] measured an elastic modulus of 78 GPa for an LS<sub>2</sub>-based glass-ceramic containing K<sub>2</sub>O, Al<sub>2</sub>O<sub>3</sub>, ZrO<sub>2</sub> and P<sub>2</sub>O<sub>5</sub>. All of these data agree with those measured in this study.

#### 4.1.2. Flexural strength

The flexural strength technique has long been a basic test to determine the resistance of ceramics and glasses to fracture [35]. However, there has been no systematic investigation of the variation of the crystallized volume fraction on the strength of LS<sub>2</sub> glass-ceramics with a constant grain size. Most of the previous studies refer to non-stoichiometric LS<sub>2</sub> glass-ceramics with additions of K, Al, Zr, P and other elements, which have a microstructure that consists mainly of elongated Li<sub>2</sub>Si<sub>2</sub>O<sub>5</sub> crystals a few micrometers in length and a crystallized volume fraction that varies from 30 to 80%. Most of the tests used three- or four-point bending or biaxial flexural strength tests. The glass-ceramic with the most studied flexural strength is the commercial EMPRESS 2™. Its reported strength varies from 250 ± 30 to 400 ± 40 MPa, depending on the surface finish, test method, sample and fixture dimensions [20,23–25,28,31,32,36–39].

Borom et al. [30] showed that the presence of the Li<sub>2</sub>Si<sub>2</sub>O<sub>5</sub> phase is responsible for the increase in strength of the LS<sub>2</sub> glass-ceramics. Höland et al. [37] argued that the “rod” shape and the interlocking microstructure, associated with the high volume fraction (~70%) of Li<sub>2</sub>Si<sub>2</sub>O<sub>5</sub> crystals, is responsible for their high strength. In their study, the crystal size was approximately 5 μm in length and 0.5 μm in diameter. Morimoto and Waraporn [39] found a sharp increase in the bending strength for samples with crystallized volume fractions greater than 67%. They also observed that the fracture strength increased linearly with crystal size, doubling the strength when compared with the parent glass for a crystal size of approximately 60 nm and a 75–80% crystallized volume fraction. Wang et al. [25] observed the highest bending strength for a P-doped glass-ceramic with a more homogeneous distribution of rod-shaped Li<sub>2</sub>Si<sub>2</sub>O<sub>5</sub> crystals. Dittmer et al. [38] also observed the greatest strength in samples with the highest crystallized volume fraction.

The results shown in Fig. 7 indicate that the flexural strength increases with  $f$ . As, in our samples, the crystal size was held constant, the increase is due solely to the increase in the crystallized volume fraction. We estimated the critical defect size for different values of  $f$ , assuming a semi-elliptical crack at the surface, as  $c = (K_{DTIC}/1.28\sigma_S)^2$  [40], where  $K_{DTIC}$  is the fracture toughness for the particular volume fraction and  $c$  is the crack radius. The calculated values are shown in Table 2. The estimated critical flaw size is 32 μm for the glass, which increases to 110 μm for the fully crystallized sample.

Because the glass has a lower fracture toughness, we also estimated the effect of the thermal residual stress. Residual stresses are always present in glass-ceramics due to thermal expansion differences between the crystalline precipitates and the glass matrix. They can be calculated using the following expression [41]:

$$\sigma_c = \frac{(\alpha_c - \alpha_g) \cdot \Delta T}{\frac{1}{3K_c} + \frac{1}{4(1-f)\mu_g} + \frac{f}{3(1-f)K_g}} \quad (5)$$

where  $\sigma_c$  is the residual stress inside the precipitate,  $\alpha$  is the linear thermal expansion,  $\mu$  is the shear modulus,  $K$  is the bulk modulus and  $f$  is the volume fraction of precipitates. The subscripts g and c refer to the glass and the crystalline phase, respectively.  $\Delta T$  is the difference between  $T_g$  (when the glass stops flowing upon cooling) and room temperature. The average residual stress in the glass matrix has the opposite sign, and is given by following the equilibrium condition:

$$f \cdot \sigma_c + (1 - f) \cdot \bar{\sigma}_g = 0 \quad (6)$$

The values of the average residual stress in the glass matrix are shown in Table 2. They increase almost linearly with  $f$  and are 32.5 MPa for the glass-ceramic with 48% crystallized volume fraction. The influence of residual stresses for a crack nucleated in the glass is considered simply by adding the calculated residual stress to the applied stress and recalculating the critical defect size considering  $K_{DTIC}$  as the fracture toughness of the glass phase. The critical defect size is calculated as  $c_g = [K_{DTIC}/1.28(\sigma_S - \bar{\sigma}_g)]^2$  and decreases from 32 μm for the glass to 6 μm for the 48% crystallized sample. Therefore, at this particular  $f$ , the critical defect size is considerably smaller than the critical defect size calculated not considering the residual stresses, which is 67 μm.

Another situation that may be present is crack nucleation in the glass phase around a precipitate due to the effects of an external stress. Green [42] calculated the critical radius of the precipitate for crack nucleation that, once nucleated, may cause the specimen's failure. In his model, the thermal residual stresses in the precipitate are considered. The critical radius  $r_c$  is given by:

$$r_c = \frac{\pi K_{IC}^2 (\alpha + 1)^5}{\alpha [2\sigma_S (\alpha + 1)^2 - \sigma_c]^2 (\alpha + 2)} \quad (7)$$

where  $\alpha$  is a geometrical parameter equal to  $\pi/2$ , and  $\sigma_S$  and  $K_{IC}$  are the experimental values for each volume fraction.

The calculated values of  $r_c$  are shown in Table 2. Even for volume fractions as low as 5%, the estimated critical radius is similar to the crystal size (6 μm). The critical radius for spontaneous crack nucleation under an applied external stress is consistently less than the existing critical

**Table 2.** Calculated critical surface semi-circular flaw sizes, average residual stress in the glass phase, critical semi-circular flaw size in the glass, critical precipitate sizes for spontaneous cracking under an external stress [42] and mean free path as a function of the crystallized volume fraction under different conditions.

$f$ (%)	Critical flaw size (μm)		Critical flaw size considering residual stresses (μm)		
	No residual stresses	$\bar{\sigma}_g$ (MPa)	Glass ( $c_g$ )	Critical radius for cracking under remote stress ( $r_c$ )	Mean free path (μm)
0	32 ± 2	0.0	32 ± 2	–	–
5	17 ± 8	3.7	15 ± 5	9 ± 3	152
16	30 ± 10	11.2	13 ± 4	8 ± 3	44
48	67 ± 8	32.5	8 ± 1	6 ± 1	9
100	110 ± 20	–	–	–	–

defects inside the glass, even when the tensile thermal residual stresses inside the glass are considered. The critical radii predicted by Eq. (7) are also in the size range of the individual crystal size of our specimens. In addition, crystals tend to cluster with increasing  $f$ , forming precipitates of larger size. There is, thus, a greater probability of spontaneous fracture under an external load. The mean free path between the crystals is also shown in Table 2 and is given as  $2d(1-f)/3f$  [43], where  $d$  is the precipitate diameter and is always larger than  $c_g$ .

There are two probable mechanisms limiting the flexural strengths of our samples: (i) propagation of cracks in the glass matrix that are helped by the residual tensile stresses; and (ii) spontaneous crack nucleation around the crystals under external stress. The former is possible because the critical crack sizes are always smaller than the mean free path between the crystals for a particular volume fraction. The latter is also possible because the critical precipitate radius is similar to the crystal size.

The increases in  $H$  and  $E$  with crystallization also have beneficial effects on the strength. The greater hardness implies that, for a constant stress, the defect size produced is smaller for a constant load. Additionally, with an increasing crystallized volume fraction, the probability of a critical defect in the glass (the weaker phase) decreases and therefore the flexural strength increases.

**4.1.2.1. Effect of pores.** A close inspection of the fully crystallized samples revealed the presence of an approximately 5% volume fraction of pores. Pores always cause a reduction in strength, which can be estimated using the empirical relation [44]:

$$\sigma_s = \sigma_{s0} \exp(-nP) \quad (8)$$

where  $\sigma_{s0}$  is the experimental strength at zero porosity,  $n$  is a constant in the range 4–7 and  $P$  is the porosity. For the fully crystallized sample, for an average  $n=5.5$ , the strength reduction is 24% when compared with a pore-free sample, which demonstrates that if pores could be avoided during crystallization, an additional increase up to approximately 20–30% would be achieved, depending on the actual value of  $n$ .

In addition to the overall porosity, it is expected that the strength does not depend on the pore size if the pores are perfectly spherical. For a spherical pore, the stress concentration factor is 3 and does not depend on its radius [45]. It is likely that some of the pores that are nucleated by degassing at the crystal/glass boundaries are not perfectly spherical, in which case the stress concentration will be a function of their size and shape.

The presence of a crystallized layer resulted in an increase, from 260 to 290 MPa, in the flexural strength of the fully crystallized samples. It is known that the residual stress in this layer is caused by the thermal expansion and elastic mismatches between the glass and the crystals. It reaches  $50 \pm 15$  MPa (compressive) for low crystallized volume fractions [9]. Because there is no glass phase in our fully crystallized materials, this difference may result from the intrinsic thermal expansion and elastic anisotropies of the  $\text{Li}_2\text{Si}_2\text{O}_5$  phase. This phase has an orthorhombic unit cell, and the crystallized surface has a tendency to grow preferentially along the  $c$ -direction [9]. Therefore, we suggest that this increased flexural strength might be due to the residual stresses (most likely slightly compressive)

caused by the thermal expansion and elastic anisotropies of the orthorhombic unit cell.

#### 4.1.3. Indentation fracture toughness

We observed an increase in the indentation fracture toughness with the crystallized volume fraction, as observed in Fig. 9. However, these data are not in agreement with the measurements of the fracture toughness measured using the double torsion technique, as shown in Fig. 14.  $K_C$  and  $K_{DTIC}$  were in agreement only for low  $f$ , below approximately 15%; for greater volume fractions, there is a continuous increase in  $K_{DTIC}$  with  $f$ .

Quinn and Bradt [46] discussed the use of the Vickers indentation technique to determine the fracture toughness of ceramic materials. Based on the reported data from studies by several authors and tests performed using different materials, they recommended that the Vickers indentation technique should be discontinued as a test to measure  $K_{IC}$ . Nevertheless, the indentation technique has several advantages: it is simple, fast and non-destructive, and requires only a small sample region with a flat and polished surface. For these reasons, several studies have reported, and continue to use, indentation fracture toughness as an estimate of the fracture toughness for many materials, including lithium-disilicate-based glass-ceramics [31,47]. However, as our results demonstrate, the indentation technique only gives approximate results for fracture toughness at very low values of  $f$ . For more crystallized samples, it predicts a significantly lower toughness, which may have several causes: internal residual stresses, changes in the crack geometry with  $f$ , and R-curve behavior.

The thermal residual stresses arise because of the thermal expansion mismatch between the glass and the crystals, which determines the crack path depending on the difference in the thermal expansions [4]. As  $f$  increases, the crack produced by the indenter may change from semicircular to Palmqvist, and different cracks with different geometries (lateral, cone or ring cracks) may be formed. These cracks relieve the residual stresses produced during the indentation, and the models of Niihara et al. and Anstis et al. are no longer valid. Additionally, polycrystalline ceramics usually show an increase in resistance to fracture for larger cracks. This behavior translates to an increase in toughness with increasing crack length. For the indentation test, this

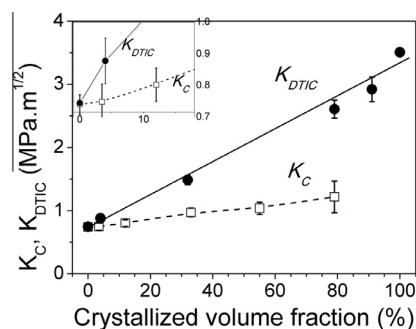


**Fig. 14.** Comparison between the indentation fracture toughness using a 10 N Vickers indentation according to Anstis et al. [13] and the fracture toughness evaluated using the double torsion technique as a function of the crystallized volume fraction for  $\text{LS}_2$  glass-ceramics with a constant crystal size (12  $\mu\text{m}$ ). The inset is a magnification of  $K_C$  and  $K_{DTIC}$  for lower values of  $f$ . The lines are a guide to the eye only.

property is equivalent to a dependence of the crack length on the indentation load and may explain why  $K_C$  is lower than  $K_{DTIC}$  for highly crystallized  $LS_2$  glass-ceramic samples.

Therefore, while the use of the indentation technique has some advantages, it does not provide true fracture toughness values, as we clearly demonstrate in Fig. 14.

#### 4.1.4. Fracture toughness

We observed a continuous increase in  $K_{DTIC}$  with  $f$  for  $LS_2$  glass-ceramics. Several factors may contribute to the increased fracture toughness of glass-ceramics: crack deflection [48], increased elastic modulus due to crystallization [49], crack bowing and trapping [43], crack bridging [50], internal residual stresses [51], pre-existing microcracking [52] and phase transformation induced by fracturing [53]. We will discuss each of these possibilities below.

**4.1.4.1. Crack deflection and elastic modulus.** The contribution of crack twist and tilt derives from the fact that, as the crack deviates from its planar configuration, modes II and III are also induced at the crack front, resulting in an increase in fracture toughness [48]. The causes of crack deviation are residual stresses due to thermal expansion, elastic mismatches between the precipitate and the matrix, and crack deflection at the precipitate/glass interface [4]. Faber and Evans [48] estimated the influence of the crystallized volume fraction, particle morphology and aspect ratio of the precipitates on the strain energy release rate for fracture. The increase in the strain energy release rate,  $G$ , of the deflected crack is

$$EG = K_I^2(1 - \nu^2) + K_{II}^2(1 - \nu^2) + K_{III}^2(1 + \nu) \quad (9)$$

where  $K_I$ ,  $K_{II}$  and  $K_{III}$  are the local stress intensity factors as a function of the deflected angle and  $E$  and  $\nu$  are the elastic modulus and Poisson's ratio of the material.

The toughening increment  $G_C$  is equal to  $(G^m / \langle G \rangle) G_C^m$ , where  $G^m$  is the strain energy release rate for an undeflected crack,  $\langle G \rangle$  is the average strain energy release rate across the crack front and  $G_C^m$  is the critical energy release rate of the matrix. The different stress intensity factors were calculated using trigonometric relations as a function of the tilt and twist angles. The toughening increment was calculated by averaging the tilt and twist components and the increase in the fracture surface area. We have calculated the toughening increment for a uniform spacing and also for a normal distribution of spheres. The standard deviation was assumed to be  $0.4(L/r_0)$ , where  $L$  is the interparticle distance and  $r_0$  is the precipitate radius. Here we used a slightly different relationship than the original used by Faber and Evans (Eq. (29) in Ref. [48]) for the normal distribution:

$$\frac{\langle G \rangle}{G^\infty} = \frac{1}{\sqrt{2\pi}} \left\{ \int_2^\infty \frac{1}{\sigma} e^{-(z-L/r_0)^2/2\sigma^2} [G^T(z) + G^t(z)] dz + \int_{-\infty}^{-2} \frac{1}{\sigma} e^{-(z-L/r_0)^2/2\sigma^2} [G^T(z) + G^t(z)] dz \right\} \quad (10)$$

where  $G^T$  and  $G^t$  are the contributions of the crack twist and tilt, respectively,  $z = x/r_0$  and  $\sigma = 0.4L/r_0$ . The precipitates are in contact for  $z = 2$ , and they do not contribute to crack deflection for  $z < 2$  because they act as a single precipitate. The results of the calculations are shown in

Fig. 15. The strain energy release rate for the experimental data was calculated as  $K_{DTIC}^2(1 - \nu^2)/E$ .

The calculated strain energy release rate assuming uniform spacing fits the experimental data for volume fractions below 10% well. For higher volume fractions,  $G_C$  is underestimated. For the Gaussian spacing distribution, the predicted strain energy release rate does not fit the experimental data well: it predicts a higher toughness at low volume fractions and a lower toughness at high volume fractions when compared with the experimental data.

Another contribution to the toughness is the elastic modulus. An increase in the elastic modulus results in an increase in the strain energy release rate. This fact can be observed from Eq. (9). If the elastic modulus of the glass-ceramics is increased, there is a decrease in the strain energy release rate. As a consequence, a greater  $G$  must be applied in order for the crack to advance and fracture the specimen. The relative increase in  $G$  is proportional to  $E_{gc}/E_g$ , where  $E_{gc}$  and  $E_g$  are the elastic moduli of the glass-ceramic and the glass, respectively.

As shown in Fig. 6(b), the crystallization of  $LS_2$  glass-ceramic causes a continuous increase in the elastic modulus, from 80 GPa in the glass to 120 GPa in the fully crystallized sample. The incorporation of the elastic modulus increase in the calculated  $G$  is also plotted in Fig. 15. There is a continuous increase in  $G_C$  with the crystallized volume fraction, and the correction is on the order of 20%.

From Fig. 12, we were able to experimentally measure the crack deflection angle distributions for the full range of crystallization from glass to a totally crystallized sample (Fig. 13(a)). Therefore, we can estimate the increase in toughness for each individual deflection distribution. To achieve this goal, we fitted a pseudo-Voigt function to each distribution in Fig. 13(a), including a normalization constant. This constant was obtained by normalization of the function over the interval  $-\pi/2$  and  $\pi/2$ . The strain energy release rate was calculated as

$$\frac{\langle G \rangle}{G^\infty} = \int_{-\pi/2}^{\pi/2} F(\phi) [G^T(\phi) + G^t(\phi)] d\phi \quad (11)$$

where  $F(\phi)$  is the fitted pseudo-Voigt function to the experimental crack deflection profile. The results are plotted in Fig. 16 as a function of the crystallized volume fraction and are compared with our experimental data. Kotoul et al. [54] proposed different trigonometric relations for  $G^T(\phi)$  and  $G^t(\phi)$  for the dependence of the stress intensity

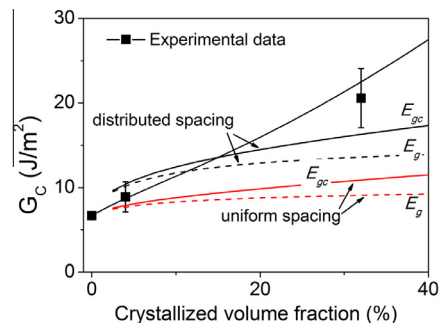
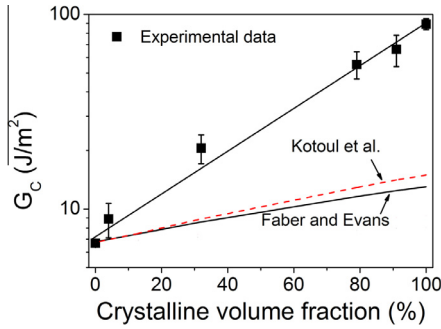


Fig. 15. Experimental data and calculated strain energy release rate due to crack tilt and twist with different crystallized volume fractions according to Faber and Evans [48]. The different effects of uniform and distributed precipitate spacing are shown. The effects of increases in the elastic modulus with  $f$  ( $E_g$  and  $E_{gc}$ ) are also shown.



**Fig. 16.** Experimental data and calculated strain energy release rate from the experimental fracture surface roughness from Fig. 13(a) according to Faber and Evans [48] and Kotoul et al. [54]. The effect of the increase in the elastic modulus with  $f$  on  $G_C$  is also shown.

factors on the crack twist and tilt angles (see Eq. (8) in Ref. [54]). The calculations using their proposed relations are also plotted in Fig. 16. In both cases, the increase in the strain energy release rate is in relation to the strain energy release rate of the glass. The maximum increase in crack toughness due to crystallization is 20% according to Faber and Evans [48] and 90% according to Kotoul et al. [54]. The relation proposed by Kotoul et al. predicts a greater toughness than those calculated according to Faber and Evans. Additionally, the inclusion of the increase in  $E$  with  $f$  does not result in a significant increase in  $G_C$ . It is clear that the crack deflection and the increase in the elastic modulus alone cannot explain the increase in  $G_C$ , which is approximately 25 times higher than the  $G_C$  of the glass.

**4.1.4.2. Crack bowing.** Another toughening mechanism is crack bowing. This has been treated by Evans et al. [52] and Green [43]. As the crack advances and encounters a precipitate, the precipitate acts as an obstacle to crack propagation, especially if the precipitate toughness is higher than the glass, as is usually observed in glass-ceramics. As the crack becomes pinned between two precipitates separated by a distance  $d$ , it bows under with increased stress to form a semielliptical shape until it breaks away at a stress  $\sigma_r$ , higher than the stress  $\sigma_C$  required for crack propagation in the glass. We observed some evidence of this in some photographs (not shown). Depending on the precipitate toughness, the crack may partially penetrate the precipitate before breaking away. A fitting parameter of the model is the ratio of the distance  $r'$  between the origin of the secondary crack at the breakaway and the primary crack front to the interprecipitate distance  $2c'$ . For strong (impenetrable) obstacles, the crack front is almost semicircular and  $r' = 2r_0$ , where  $r_0$  is the precipitate radius. For weak (penetrable) obstacles, the crack front is straighter, and the ratio  $r'/r_0$  is less than 1 and defines the strength of the obstacle. Green [43] fitted the ratio  $\sigma_r/\sigma_C$  as a function of  $r'/c'$  using a series expansion. The increase in toughness is defined as

$$\frac{G_C}{G_g} = \frac{E_g}{E_{gc}} \left( \frac{\sigma_r}{\sigma_C} \right)^2 \quad (12)$$

where  $G_g$  is the glass strain energy release rate.

A critical parameter in the model is the interparticle distance  $2c'$ . For strong obstacles, it has been suggested that, for a random distribution of spheres,  $2c' = (\sqrt{2\pi/3f} - 2)r_0$ . For weak obstacles, the interparticle dis-

tance is equal to the mean free path and  $2c' = 4r_0(1 - f)/3f$ .

The influence of crack bowing according to Green [43] is plotted in Fig. 17 as a function of the crystallized volume fraction for strong and weak obstacles with different strengths. For the case of LS<sub>2</sub> glass-ceramics, the strong obstacles predict a much greater fracture toughness than experimentally observed. The best fit is for weak obstacles with a strength of  $r'/r_0 = 0.4$ , although it overestimates the toughness at low volume fractions.

**4.1.4.3. Crack bridging and trapping.** A more detailed calculation that considers not only crack bowing and trapping but also bridging was performed by Bower and Ortiz [50] for low crystallized volume fractions. They considered a rectangular array of perfectly bonded particles, as is the case in glass-ceramics. If  $K_{IC}^p/K_{IC}^g < 3$ , where  $K_{IC}^p$  and  $K_{IC}^g$  are the critical stress intensity factors of the crystals and the glass, respectively, the crack is able to penetrate the precipitates and fracture them, and no bridging is formed. If  $K_{IC}^p/K_{IC}^g > 7$ , the crack bypasses the precipitates, bridging the surfaces behind the crack. A more detailed description of the different mechanisms is shown in Fig. 18, where  $r_0$  is the precipitate radius and  $L$  is the particle distance [50]. These two parameters are related to the volume fraction of the (assumed) spherical particles by  $r_0/L = \sqrt{3f/2\pi}$ .

From a previous section,  $K_{DTIC}^p/K_{DTIC}^g = 5$  for LS<sub>2</sub>. Therefore, Fig. 18 shows that, as the crystallized volume fraction increases, the crack is able to bypass the precipitates in a succession of unstable bridging and stable pinning

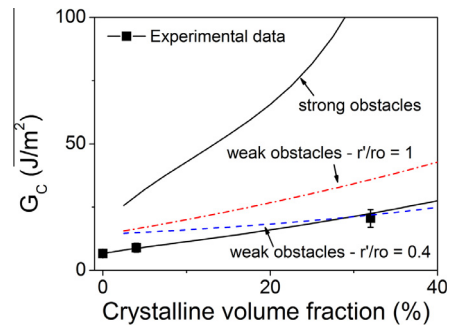


**Fig. 17.** Influence of crack bowing and trapping on the strain energy release rate according to Green [43] for strong and weak obstacles with different strengths compared with the experimental data.

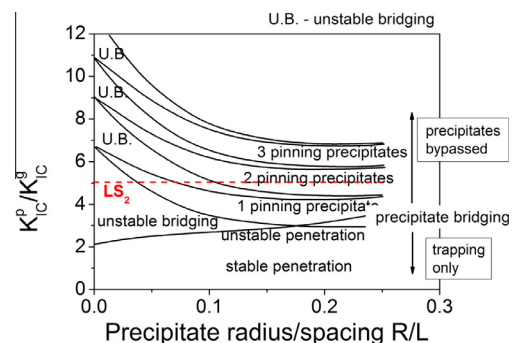


**Fig. 18.** Different regimes of a crack interacting with bonded precipitates according to Bower and Ortiz [50]. A line corresponding to  $K_{IC}^p/K_{IC}^g = 5$  for LS<sub>2</sub> is indicated in the figure. Adapted from Ref. [50].

precipitate regimes. Unstable bridging occurs when the crack bypasses the precipitates, but they fracture before the crack reaches the next row of precipitates. For very low crystal volume fractions, approximately 2% ( $r_0/L = 0.1$ ), there are already two rows of bridging precipitates, which remain the same up to a volume fraction of approximately 13% ( $r_0/L = 0.25$ ). Therefore, under these conditions, there is a regime of both crack trapping and crack bridging.

For this condition, Bower and Ortiz [50] estimated the increase in toughness due to crack trapping and bridging as

$$\frac{K_{IC}^{gc}}{K_{IC}^g} = \sqrt{1 + \pi \left(\frac{r_0}{L}\right)^2 \left[ \left(\frac{K_{IC}^p}{K_{IC}^g}\right)^2 - 1 \right]} \quad (13)$$

where  $K_{IC}^{gc}$  is the critical stress intensity factor of the glass-ceramic.

The result of the calculation is shown in Fig. 19. The predicted toughness is greater than the experimental data.

Because the bonding between the crystalline precipitates and the glass matrix is very good in glass-ceramics in general, and especially in LS<sub>2</sub>, where the precipitate and the glass are stoichiometric, no frictional crack bridging is observed, which is another important toughening mechanism in ceramics that was not observed here.

#### 4.1.4.4. Fracture toughness variation as a function of crystallized volume fraction.

All of the models shown earlier are valid for low crystallized volume fractions. As the volume fraction increases and the precipitates become closer to one another, a crack is not able to bow out completely before contacting the next precipitate. Additionally, we observed in our LS<sub>2</sub> glass-ceramics that some precipitates also fractured, even at low crystallized volume fractions, and thus their toughness should be incorporated in the model. To include the crystal toughness and extend the ability to predict toughness to higher crystallized volume fractions, we will treat this problem in a simplified manner.

Consider a crack that advances towards an area  $A_T$  in the crack plane. This area will be composed of an area  $A_P$  from the precipitates and an area  $A_G$  from the glass, such that  $A_T = A_P + A_G$ . The work performed per unit area to fracture the glass-ceramic will be the sum of the work performed per unit area of fracturing the glass and the precipitates:

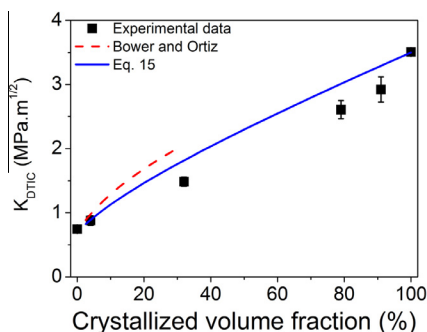


Fig. 19. Experimental and calculated toughness for the influence of crack trapping and bridging on the fracture toughness according to Bower and Ortiz [50] and according to Eq. (15).

$$\frac{(1 - v_{gc}^2)}{E_{gc}} (K_{IC}^{gc})^2 A_T = \frac{(1 - v_p^2)}{E_p} (K_{IC}^p)^2 A_P + \frac{(1 - v_g^2)}{E_g} (K_{IC}^g)^2 (1 - A_P) \quad (14)$$

The ratio  $A_P/A_T$  is assumed to be proportional to the crystallized volume fraction  $f$  and, as there is no significant difference between the Poisson's modulus of the glass and the precipitate, the result is

$$K_{IC}^{gc} = K_{IC}^g \sqrt{\frac{E_{gc}}{E_g} + f \cdot \left( \frac{E_{gc}}{E_p} \cdot \left(\frac{K_{IC}^p}{K_{IC}^g}\right)^2 - \frac{E_{gc}}{E_g} \right)} \quad (15)$$

where the elastic modulus of the glass-ceramic,  $E_{gc}$ , was taken as the best fitting line of Fig. 6(b). This procedure results in an upper bound from the rule of mixtures for fracture toughness.

The results are plotted in Fig. 19. The experimental data are only slightly lower than the prediction of Eq. (15). Several factors affect the crack path: precipitate morphology and size, elastic mismatch between the precipitate and glass, thermal residual stresses, glass and precipitate fracture toughness and interfacial strength [4,55–57]. One possibility for the difference observed in Fig. 19 is the tendency for the crack to propagate more in the weaker phase (glass) than in the tougher phase (precipitates) at moderate crystallized volume fractions. At crystallized volume fractions between 30 and 70%, the glass and the precipitates form two interpenetrable phases as they are within the percolation limits. In LS<sub>2</sub> glass-ceramics, the thermal expansion of the glass is higher than the precipitate and tensile residual stresses are developed in the glass phase (and compressive stresses in the precipitates). The consequence is that the actual ratio of the glass crack surface area to the total surface crack area  $A_G/A_T$  is larger than  $(1 - f)$ , where  $f$  is measured by the usual method of the area analysis of a polished area of the glass-ceramic. Also, the ratio  $A_P/A_T$  is smaller than  $f$  and Eq. (15) overestimates  $K_{IC}^{gc}$ .

To further treat this problem, we defined the ratio  $A_P/A_T$  of the crack surface as  $f'$  to be used in Eq. (15). The measurement of  $f'$  is difficult and an estimative of  $f'$  from  $f$  would be beneficial. We proposed the simple relation:

$$f' = \frac{\xi \cdot f}{1 + \xi - f} \quad (16)$$

where  $\xi$  is an adjustable parameter. Eq. (16) has some advantages. At both limits, when  $f$  is 0 (glass) or 1 (fully crystallization),  $f' = f$ . Also, if  $\xi \rightarrow \infty$ ,  $f' = f$  for all  $f$  and Eq. (15) is recovered. Finally, the smaller  $\xi$  is, the more different  $f'$  is from  $f$ . Fig. 20 shows Eq. (16) evaluated for different values of  $\xi$ . Eq. (16) is inspired by the semi-empirical Halpin–Tsai equation used to estimate the elastic constants for two-phase elastic solids [58].

When  $f'$  defined by Eq. (16) is substituted in Eq. (15), we have:

$$K_{IC}^{gc} = K_{IC}^g \sqrt{\frac{E_{gc}}{E_g} + \frac{\xi \cdot f}{(1 + \xi - f)} \cdot \left( \frac{E_{gc}}{E_p} \cdot \left(\frac{K_{IC}^p}{K_{IC}^g}\right)^2 - \frac{E_{gc}}{E_g} \right)} \quad (17)$$

A best fit using the least-squares method of Eq. (17) for the experimental data yields  $\xi = 1.74$ . The result is plotted in Fig. 21. The agreement with the experimental data is very

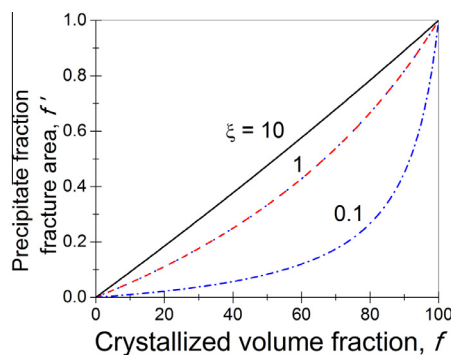


Fig. 20. The ratio of the precipitates area to the total area of the crack surface  $f'$  as a function of the crystallized volume fraction  $f$  according to Eq. (16).

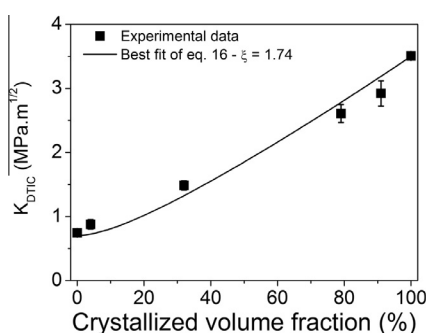


Fig. 21. A minimum least-squares fit of Eq. (17) to the experimental data with  $\xi = 1.74$ .

good, covering the full range from the parent glass to the fully crystallized glass-ceramic.  $\xi$  defines how close the precipitate fraction crack area  $f'$  is to the crystallized volume fraction  $f$ , and is the only adjustable parameter of the model.

Internal residual stresses have always been thought to affect fracture toughness. In  $LS_2$  glass-ceramics, the crystal thermal expansion is lower than that of glass. Therefore, residual tensile stresses are present in the tangential direction in the glass matrix and, according to Taya et al. [51], its contribution would be to decrease the fracture toughness with increasing  $f$ . However, this result contradicts the experimental observations in this work. A similar situation was observed in a bioglass-ceramic of the Na–Ca–Si–P–O system, where the crystalline phase has a lower thermal expansion than that of the glass and an increase in fracture toughness with crystallization was experimentally observed [1]. Therefore, residual stresses have a negligible direct effect on the fracture toughness in these  $LS_2$  glass-ceramics.

Rouxel and Laurent [59] studied the mechanical properties of an oxynitride glass with dispersed SiC particles. The maximum SiC volume fraction studied was 40%. Their composite showed an increase in strength and fracture toughness with  $f$ , which was attributed to crack bowing and bridging due to the strong interfacial bonding between the glass and the particles, and also due to the higher  $E$ , fracture strength and  $K_{IC}$  of the SiC particles.

Finally, phase transformations did not contribute to the fracture toughness because no phase transformation was observed for the  $Li_2Si_2O_5$  phase in  $LS_2$  glass-ceramics.

## 5. Conclusions

We measured several mechanical properties of stoichiometric lithium disilicate glass-ceramics by systematically varying the crystallized volume fraction from 0 to 100% while keeping the crystal size constant. Controlled internal crystallization of lithium disilicate glass significantly increased the hardness, elastic modulus, flexural strength and fracture toughness. All of these properties reached a maximum for the fully crystallized glass-ceramic.

The hardness and elastic modulus increase linearly with the crystallized volume fraction. The values of the indentation fracture toughness were much lower than the real fracture toughness measured using the double torsion technique. The flexural strength showed a strong increase for low crystallized volume fractions,  $f$ , then slowly increased with greater  $f$ . The controlling factor of the flexural strength of the partially crystallized glass-ceramics appears to be pre-existing cracks in the glass matrix (subjected to residual tensile stresses) and the cracking of the glass matrix around the precipitates when subjected to external loading.

The distributions of the crack deflection angles were experimentally measured and their contribution to crack toughening was estimated. We then calculated the possible contributions of several mechanisms and concluded that the main toughening mechanisms are crack bowing and trapping (for low  $f$ ), as well as the greater elastic modulus and fracture toughness of the crystal precipitates. A simple model, which incorporates the elastic moduli, precipitate fracture toughness and crystallized volume fraction, was proposed to explain the evolution of fracture toughness with crystallized volume fraction. The agreement with experimental data was very good. Although these results refer to  $LS_2$ , we expect them to apply to several other types of glass-ceramics.

## Acknowledgements

The authors are grateful to the Brazilian funding agencies CNPq, CAPES and Fundação Araucária for financial support, C-LABMU/UEPG for the use of research facilities, Arotec/Olympus for the laser confocal microscopy measurements and Dr. C.M. Lepienski for the instrumented indentation tests. E.D.Z. thanks the São Paulo Research Foundation – FAPESP for CEPID grant 2013/07793-6. The authors are indebted to Prof. J.J. Mecholsky Jr. for his valuable critical comments.

## References

- [1] O. Peitl, E.D. Zanotto, F.C. Serbena, L.L. Hench, *Acta Biomater.* 8 (2012) 321.
- [2] F.C. Serbena, G.P. Souza, E.D. Zanotto, J. Lumeau, L. Glebova, L.B. Glebov, *J. Am. Ceram. Soc.* 94 (2011) 671.
- [3] F.C. Serbena, V.O. Soares, O. Peitl, H. Pinto, R. Muccillo, E.D. Zanotto, *J. Am. Ceram. Soc.* 94 (2011) 1206.
- [4] F.C. Serbena, E.D. Zanotto, *J. Non-Cryst. Solids* 358 (2012) 975.
- [5] E.D. Zanotto, *Am. Ceram. Soc. Bull.* 89 (2010) 19.
- [6] W. Höland, V. Rheinberger, E. Apel, C. Van't Hoen, *J. Eur. Ceram. Soc.* 27 (2007) 1521.
- [7] S.W. Freiman, L.L. Hench, *J. Am. Ceram. Soc.* 55 (1972) 86.
- [8] V.R. Mastelaro, E.D. Zanotto, *J. Non-Cryst. Solids* 247 (1999), 79±86.

- [9] H. Pinto, L. Ito, M. Crovace, E.B. Ferreira, F. Fauth, T. Wroblewski, E.D. Zanotto, A.R. Pyzalla, J. Non-Cryst. Solids 353 (2007) 2307.
- [10] C.A. Schneider, W.S. Rasband, K.W. Eliceiri, Nat. Methods 9 (2012) 671.
- [11] W.C. Oliver, G.M. Pharr, J. Mater. Res. 7 (1992) 1564.
- [12] K. Niihara, R. Morena, D.P.H. Hasselman, J. Mater. Sci. Lett. 1 (1982) 13.
- [13] G.R. Anstis, P. Chantikul, B.R. Lawn, D.B. Marshall, J. Am. Ceram. Soc. 64 (1981) 533.
- [14] M.A. Meyers, K.K. Chawla, Mechanical Behavior of Materials, second ed., Cambridge University Press, Cambridge, 2008.
- [15] A.G. Evans, J. Mater. Sci. 7 (1972) 1137.
- [16] M.A. Madjoubi, M. Hamidouche, N. Bouaouadja, J. Chevalier, G. Fantozzi, J. Mater. Sci. 42 (2007) 7872.
- [17] D. Williams, A. Evans, J. Test. Eval. 7 (1974) 44.
- [18] A. Shyam, E. Lara-Curzio, J. Mater. Sci. 41 (2006) 4093.
- [19] P.C. Soares, E.D. Zanotto, V.M. Fokin, H. Jain, J. Non-Cryst. Solids 331 (2003) 217.
- [20] S. Huang, P. Cao, C. Wang, Z. Huang, W. Gao, J. Asian Ceram. Soc. 1 (2013) 46.
- [21] B. De Jong, P.G.G. Slaats, H.T.J. Super, N. Veldman, A.L. Spek, J. Non-Cryst. Solids 176 (1994) 164.
- [22] S.B. Massardo, Nanoindentação em vitrocerâmicas de dissilicato de lítio – fractografia e propriedades mecânicas (PhD thesis), Universidade Federal do Paraná, 2010.
- [23] G. Wen, X. Zheng, L. Song, Acta Mater. 55 (2007) 3583.
- [24] M.J. Cattell, R.P. Palumbo, J.C. Knowles, R.L. Clarke, D.Y.D. Samarawickrama, J. Dent. 30 (2002) 161.
- [25] F. Wang, J. Gao, H. Wang, J. Chen, Mater. Des. 31 (2010) 3270.
- [26] S. Buchner, C.M. Lepienski, P.C. Soares Jr., N.M. Balzaretto, Mater. Sci. Eng. A 528 (2011) 3921.
- [27] M. Guazzato, M. Albakry, S.P. Ringer, M.V. Swain, Dent. Mater. 20 (2004) 449.
- [28] D.U. Tulyaganov, S. Agathopoulos, I. Kansal, P. Valério, M.J. Ribeiro, J.M.F. Ferreira, Ceram. Int. 35 (2009) 3013.
- [29] S. Huang, B. Zhang, Z. Huang, W. Gao, P. Cao, J. Mater. Sci. 48 (2013) 251.
- [30] M.P. Borom, A.M. Turkalo, R.H. Doremus, J. Am. Ceram. Soc. 58 (1975) 385.
- [31] H. Fischer, R. Marx, Dent. Mater. 18 (2002) 12.
- [32] M. Albakry, M. Guazzato, M.V. Swain, J. Prosthet. Dent. 89 (2003) 374.
- [33] E. Apel, J. Deubener, A. Bernard, M. Höland, R. Müller, H. Kappert, V. Rheinberger, W. Höland, J. Mech. Behav. Biomed. Mater. 1 (2008) 313.
- [34] J. Deubener, M. Höland, W. Höland, N. Janakiraman, V.M. Rheinberger, J. Mech. Behav. Biomed. Mater. 4 (2011) 1291.
- [35] G.D. Quinn, B.T. Sparenberg, P. Koshy, L.K. Ives, S. Jahanmir, D.D. Arola, J. Test. Eval. 37 (2009) 222.
- [36] I. Denry, J.A. Holloway, Materials 3 (2010) 351.
- [37] W. Höland, M. Schweiger, M. Frank, V. Rheinberger, J. Biomed. Mater. Res. 53 (2000) 297.
- [38] M. Dittmer, C. Ritzberger, M. Schweiger, V. Rheinberger, M. Wörle, W. Höland, J. Non-Cryst. Solids 384 (2014) 55, <http://dx.doi.org/10.1016/j.jnoncrysol.2013.03.009>.
- [39] S. Morimoto, E. Waraporn, J. Ceram. Soc. Jpn. 112 (2004) 259.
- [40] J. Newman Jr, I. Raju, Eng. Fract. Mech. 15 (1981) 185.
- [41] C.-H. Hsueh, P.F. Becher, Mater. Sci. Eng. A 212 (1996) 22.
- [42] D.J. Green, J. Am. Ceram. Soc. 64 (1981) 138.
- [43] D.J. Green, J. Am. Ceram. Soc. (1983), 66:C.
- [44] W.D. Kingery, H.K. Bowen, D.R. Uhlmann, Introduction to Ceramics, second ed., Wiley-Interscience, New York, 1976.
- [45] T.L. Anderson, Fracture Mechanics: Fundamentals and Applications, third ed., CRC Press, Boca Raton, FL, 2004.
- [46] G.D. Quinn, R.C. Bradt, J. Am. Ceram. Soc. 90 (2007) 673.
- [47] M. Albakry, M. Guazzato, M.V. Swain, J. Dent. 31 (2003) 181.
- [48] K.T. Faber, A.G. Evans, Acta Metall. 31 (1983) 565.
- [49] R.I. Todd, A.R. Boccaccini, R. Sinclair, R.B. Yaltee, R.J. Young, Acta Mater. 47 (1999) 3233.
- [50] A.F. Bower, M. Ortiz, J. Mech. Phys. Solids 39 (1991) 815.
- [51] M. Taya, S. Hayashi, A.S. Kobayashi, H.S. Yoon, J. Am. Ceram. Soc. 73 (1990) 1382.
- [52] A.G. Evans, H. Heuer, D.L. Porter, The fracture toughness of ceramics, in: D.M.R. Taplin (Ed.), Fracture, vol. 1, University of Waterloo Press, Ontario, Canada, 1977, pp. 529–556.
- [53] A.G. Evans, J. Am. Ceram. Soc. 73 (1990) 187.
- [54] M. Kotoul, J. Pokluda, P. Sandera, I. Dlouhý, Z. Chlup, A.R. Boccaccini, Acta Mater. 56 (2008) 2908.
- [55] M.Y. He, A.G. Evans, J.W. Hutchinson, Int. J. Solids Struct. 31 (1994) 3443.
- [56] Y. Li, M. Zhou, J. Mech. Phys. Solids 61 (2013) 472.
- [57] Y. Li, M. Zhou, J. Mech. Phys. Solids 61 (2013) 489.
- [58] J.C. Halpin, J.L. Kardos, Polym. Eng. Sci. 16 (1976) 344.
- [59] T. Rouxel, Y. Laurent, Int. J. Fract. 91 (1998) 83.